SPE 36698

Three-Dimensional Geomechanical Simulation of Reservoir Compaction and Implications for Well Failures in the Belridge Diatomite

J.T. Fredrich, SPE, J.G. Argüello, B.J. Thorne, and W.R. Wawersik, SPE, Sandia National Laboratories; G.L. Deitrick and E.P. de Rouffignac, SPE, Shell E&P Co.; L.R. Myer, Lawrence Berkeley National Laboratory; M.S. Bruno, SPE, Terralog Technologies

This paper was prepared for presentation at the 1996 SPE Annual Technical Conference and Exhibition held in Denver, Colorado, U.S.A., 6–9 October 1996.

Abstract

This paper describes an integrated geomechanics analysis of well casing damage induced by compaction of the diatomite reservoir at the Belridge Field, California. Historical data from the five field operators were compiled and analyzed to determine correlations between production, injection, subsidence, and well failures. The results of this analysis were used to develop a three-dimensional geomechanical model of South Belridge, Section 33 to examine the diatomite reservoir and overburden response to production and injection at the interwell scale and to evaluate potential well failure mechanisms. The time-dependent reservoir pressure field was derived from a three-dimensional finite difference reservoir simulation and used as input to three-dimensional non-linear finite element geomechanical simulations. The reservoir simulation included ~200 wells and covered 18 years of production and injection. The geomechanical simulation contained 437,100 nodes and 374,130 elements with the overburden and reservoir discretized into 13 layers with independent material properties. The results reveal the evolution of the subsurface stress and displacement fields with production and injection and suggest strategies for reducing the occurrence of well casing damage.

Introduction

Well casing damage induced by formation compaction has occurred in reservoirs in the North Sea, the Gulf of Mexico, California, and Asia.[1-4] As production draws down reservoir pressure, the weight of the overlying formations is increasingly supported by the solid rock matrix that compacts in response to the increased stress. The diatomite reservoirs of Kern County, California are particularly susceptible to depletion-induced compaction because of the high porosity (45-70%) and resulting high compressibility of the reservoir rock.

The Belridge Field, located about 45 miles west of Bakersfield, California, recently attained billion-barrel status and is currently the fifth most productive field in the US.[5] The thickness (more than 1000 feet), high porosity, and moderate oil saturation of the diatomite reservoir translate into huge reserves, with more than 3 billion bbl of original-oil-in-place estimated for the Belridge Field. However, 75% of production to date has been from the overlying Tulare sands.

Production from the diatomite reservoir is hampered by the unusually low matrix permeability (~0.1 mDa or less). Although the Belridge Field was discovered in 1911, production from the diatomite reservoir became economical only with the introduction of hydraulic fracturing stimulation techniques in the mid-1970's.[6] However, increased production decreased reservoir pressure, accelerated surface subsidence, and increased the number of costly well failures in the 1980's. Waterflood programs were initiated in the late 1980's to combat the reduced well productivity, accelerated surface subsidence, and subsidence-induced well failure risks. Subsidence rates are now near zero; however, the well failure rate, although lower than that experienced in the 1980's, is still economically significant at 2-5% of active wells per year.

In 1994 a cooperative research program was undertaken to improve understanding of the geomechanical processes leading to well casing damage during production from weak, compactable formations. The study focuses on the Belridge Field and represents a significant extension of earlier work in two regards. First, a comprehensive data base was compiled to provide a unique, complete picture of the reservoir and overburden behavior.[7] Second, the results of the field-wide analysis motivated large-scale three-dimensional numerical simulations. Previous numerical studies of drawdown-induced compaction and subsidence at South Belridge[8,9] included only two-dimensional plane strain approximations that could not

capture the locally complex production, injection, and subsidence patterns indicated by the field-wide data analysis.

Reservoir Geology

The Belridge Field is developed on two elongated northwestward-trending anticlines (**Fig. 1**) that are structurally offset by the Middle Belridge fault.[10-12] In this paper, the term Belridge Field is used collectively to include development on both the northern (North Belridge) and southern (South Belridge) anticlines. Structural deformation and faulting in the area is related to the San Andreas fault zone that lies to the west. The field contains two hydrocarbon reservoirs that are produced independently of one another: the diatomite reservoir (as used here, this includes both diatomite and porcelanite lithologies), and the overlying Tulare reservoir.

The diatomite reservoir produces 10-34° gravity oil from depths of about 800 to 3000 feet, depending upon structural position. Original-oil-in-place in the diatomite is estimated at more than 2 billion bbl. The most productive interval is the Belridge Diatomite, part of the Reef Ridge Member of the prolific Monterey Formation (Miocene age) that acts as both source and reservoir rock for oil and gas deposits throughout coastal and central California.

The diatomite is a biogenic siliceous deposit consisting of the shells or tests of diatoms with varying amounts of detrital material (principally clay and sand) so that the rock ranges from fairly pure to shaley diatomite. Individual depositional cycles are identifiable, and some cycles not preserved in southern South Belridge are present in northern South Belridge and North Belridge. In the upper intervals, the diatoms are preserved as opal-A, which is an amorphous, colloidal form of silica. Average rock porosities range from 50-70%. With increasing depth (pressure) and temperature, the mineralogic phase changes from opal-A to opal-CT. This diagenetic boundary separates the Brown Shale unit of the McLure Member from the Belridge Diatomite unit of the Reef Ridge Member. The associated reduction in bulk porosity (to 45% or less) makes the diatomite reservoir significantly less productive below the opal-CT transition. Below this, the diatom skeletal structures are no longer well preserved and the rock is a porcelanite.

The diatomite is unconformably overlain by the Plio-Pleistocene-aged Tulare Formation on the crest and by the Pliocene-aged Etchegoin and San Joaquin Formations on the flanks (Fig. 1). The Tulare is the second main reservoir at Belridge and produces 11-14° gravity oil from multiple, highly discontinuous reservoir sands totaling about 400-1500 feet in thickness.[13] Current thermal recovery methods are projected to recover 50-60% of the more than 1 billion bbl estimated original-oil-in-place. The sands were deposited in a prograding fluviodeltaic depositional setting and exhibit several distinct lithofacies. Mudstones are present as laterally continuous, discrete beds (tens of feet thickness) separating the major sand intervals as well as at the interface between the Tulare and Belridge Diatomite. Mudstones are also present as thin beds (inches thickness) within individual sands. Overlying the Tulare is 100-200 feet of unsaturated alluvium (Fig. 1).

Production, Injection, Subsidence, and Well Failures

The Belridge diatomite is currently being produced by five operators: CalResources LLC, Mobil E&P Co., Santa Fe Energy Resources, Exxon Co. USA, and Crutcher-Tufts Prod. Co. (**Fig. 2**). Cal Resources, Mobil, Santa Fe, and Exxon also produce the overlying Tulare from separate wells using a combination of steam flooding and cyclic steaming.

Development History. The diatomite reservoir received renewed attention in the 1970's with the introduction of hydraulic fracturing technology.[6] However, due to the exceptionally high compressibility and thickness of the producing diatomite interval, increased production resulted in significant reservoir compaction. By 1987, nearly 20 feet of cumulative surface subsidence was estimated in some portions of the field and more than 100 wells were being abandoned annually because of severe casing damage. Waterflood programs were initiated in the late 1980's to mitigate subsidence, to reduce the potential for additional well failures, and for secondary recovery.

The low permeability of the diatomite (less than 0.1 mDa) has led to very tight development with typical well spacings of 2½ acre (330 feet) to ⅝ acre (82.5 feet). Multiple hydraulic fracture treatments are conducted in both production and injection wells with typical fracture heights and lengths (tip-to-tip) of 100-300 and 200-300 feet, respectively. Production wells are usually completed in both the diatomite and upper porcelanite intervals. All five operators are conducting pressure maintenance programs, with the exception of CalResources' leases in Middle and North Belridge that are still on 2½ acre primary development (Fig. 2).

Data Analysis. Production, injection, subsidence, and well failure data from the five operators were converted into a common coordinate system and time frame for analysis and for input to a three-dimensional visualization system.[7] The data base includes production (oil, water, and gas) and injection data for more than 3500 wells for 1984-94. The earliest available subsidence data are from 1985, but much of the field had incomplete survey monument coverage until the early 1990's. The database includes 861 damaged wells, with failure depths known for about 750 of these wells. Many, but not all, of these wells exhibited casing damage severe enough to render the well incapable of producing or injecting fluids. Some of the well failures were associated with unsuccessful conversion from production to injection.

Fig. 3 shows cumulative production, net voidage

(produced minus injected fluids), and well failures per year for all five operators. Net voidage reached a peak in 1986-87; however, the peak in well failures occurred somewhat later in 1987-89. Of substantial concern is that the well failure rate has not declined since 1992, even though all operators had pressure maintenance programs in place in heavily developed parts of the field by the late 1980's. Instead, a fairly constant well failure rate of 2-5% of active wells per year has been maintained even though subsidence has been largely arrested.

The distribution of well failures with depth is shown in **Fig. 4**. To correct for the variation in structural depth across the field, failure depths have been scaled so that the interface between the diatomite reservoir and overburden is equal to zero. More than 90% of all well casing damage to date has been above the diatomite reservoir. Damage has been focused at two particular intervals: at the interface between the diatomite and overlying Tulare Formation and at a second horizon 300-400 feet above the diatomite reservoir. Overall, there is a prominent shift in the relative percentage of failures at these two horizons such that proportionally more failures occur at the diatomite-Tulare interface after ~1990 as compared to before. However, this trend is apparent only for the CalResources and Crucher-Tufts leases, but not for the Mobil or Exxon properties (depths of damage for the Santa Fe wells were not available).

The well failures are not distributed uniformly in space on the field-scale. Instead, they are concentrated in southern (Mobil and CalResources leases) and northern (Exxon and Santa Fe leases) South Belridge and in the Crutcher-Tufts lease in North Belridge. However, the failures are uniformly distributed on the local scale. That is, in regions that experienced significant subsidence, well failures occur throughout the produced area rather than just along the perimeter or in the center of the subsiding region.[7]

Three-Dimensional Numerical Simulation of Reservoir Behavior During Production and Injection

Based upon the analysis of the unique field-wide data base, a detailed geomechanical model of South Belridge, Section 33 was formulated to evaluate potential well failure mechanisms. In particular, we considered the following: (1) Well failures have not been eliminated by the pressure maintenance programs but have continued at an economically significant rate. Current well failure rates in some parts of the field are now close to the maximum rate experienced prior to the waterflood. (2) The spatial distribution of well failures with respect to observed surface subsidence suggests that well damage is influenced by local production and injection patterns. This is consistent with the observation that a number of wells have failed within 6 months to 1 year of operation. (3) Damage is concentrated at the interface between the diatomite reservoir and overburden and at a second interface in the overburden. (4) Field observations of sheared wells indicate that lateral offsets of up to a foot can occur over very short vertical distances (tens of feet).

These observations motivated development of a model to examine the role of local gradients in effective stress in inducing well casing damage.[9] The gradients in effective stress result from large gradients in pore pressure induced by aggressive production and injection in a low permeability reservoir (well spacings ranging from 2½ to ⅝ acre). A three dimensional reservoir simulation was performed to calculate the time-dependent reservoir pressure which was then input into a three-dimensional finite element geomechanical model to examine the evolution of the subsurface stress and displacement fields with production and injection. South Belridge, Section 33 was selected since this region of the field had been the focus of previous two-dimensional finite element studies.[8,9] Therefore material models for the overburden and reservoir rock as well as the initial stress state were available.

Mechanisms for Well Casing Damage. Various mechanisms for casing damage are recognized, including compression, tension, and shear.[1-3,8,9] Compressional failures can be induced within the producing interval due to large vertical strains associated with compaction. Tensional failures can result from the elastic mismatch between the compacting reservoir and the stiffer overburden that resists subsidence as the reservoir compacts. Shear, or dog-leg, failures can be induced either by large horizontal displacements along the flanks of a subsidence bowl or possibly by local slip along weak bedding planes or reactivated faults in the overburden above the reservoir.

At the Belridge Field, compressional failures at depths as great as 1800 feet have been observed. However, as discussed above, the majority of the failures occur either at the interface between the diatomite reservoir and overburden or at a second horizon 300-400 feet higher in the overburden. Field observations indicate that both shear (dog-leg) and tensile failures occur in the overburden.

Section 33 Reservoir Model. The reservoir fluid flow simulation covers virtually the entire north-south extent of the development in Section 33 (Fig. 2). The simulation spans an area 2078 feet by 3409 feet, includes 197 production and injection wells, and covers 18 years of production history from 1978 to 1995. Nearly a hundred wells in this area have experienced significant casing damage.

Thirteen depositional cycles are identifiable within the diatomite reservoir, and transitions within many of these cycles divide them further into subcycles. Subcycles that pinch out as the crest is approached are grouped with the topmost cycle that does not, resulting in a 28 layer reservoir description. Structure, porosity, and initial oil saturation inferred from well logs were mapped by layer, and oil gravity measured from sidewall core samples was generally mapped by cycle. For the Section 33 model, the 28 layers were lumped to 9 layers (mostly by cycle), and the resulting property maps were

interpolated to define the structure, porosity, oil saturation, and oil gravity for the reservoir simulation. Gas saturation was set uniformly to 5%. Permeability was defined by permeability-porosity correlations determined from experimental measurements on core samples. Relative permeabilities (oil/water and gas/oil) were derived from previous two-dimensional reservoir simulations that were history matched to different portions of the field and were varied layer-by-layer according to each layer's maximum initial oil saturation.

The areal grid was 149×69, for a volumetric total of 92,529 gridblocks. The three-dimensional fluid flow calculation was performed using the black oil version of MORE® (Reservoir Simulation Research Corporation). Oil gravity variations were modeled using temperature-dependent PVT tables spanning a narrow temperature range. Wells with hydraulic fractures, assumed to be uniformly oriented N11E (parallel to the model boundaries) and with a tip-to-tip length of 250 feet, were modeled by completing the well in each gridblock intersected by the fracture. Quarterly liquid production/injection rate constraints were set according to each well's production history. Producing and injecting bottomhole pressure constraints were 50 and ~1100 psi, respectively.

The simulation was compared to the historical field performance (**Fig. 5**) which indicates that primary production volumes are reasonably well matched. However, the match is degraded during the early stages of the waterflood (1987-89), where the model cannot accommodate the large injected water volumes. The maximum allowed injection pressures were set higher than the field values in an attempt to better match the field injection rates.

Section 33 Geomechanical Model. To examine the influence of the production- and injection-induced pressure changes, the three-dimensional finite difference reservoir simulation was coupled to a three-dimensional non-linear finite element geomechanical model. The geomechanical model was formulated so that the reservoir flow model forms a subset of the geomechanical model such that the time-dependent pressures defined for each of the gridblocks in the finite difference calculation are directly mapped to the appropriate nodes in the finite element simulation.

The geomechanical model contains 437,100 nodal points with 374,130 eight-node Lagrangian uniform-strain elements. The simulations were performed using Sandia's three-dimensional large-deformation quasi-static structural mechanics code JAS3D. The code is a hybrid of the Sandia codes SANTOS[14] and JAC[15] that employ unique iterative (explicit) solution procedures to achieve a high degree of computational efficiency which therefore enables the analysis of extremely large and complex models such as that considered here.

Structure. The geomechanical model, which was meshed directly from geologic structure maps of Section 33, contains thirteen stratigraphic layers with independent material properties. Overall, the model is about 2100 feet wide by 10,700 feet long, and 4500 feet in depth. The east-west extent of the model (2100 feet) exactly corresponds to the east-west extent of the reservoir flow. The development to the east and west of the flow model boundaries is similar to that within the model area whereas there is no development to the north and south. Thus, to remove boundary effects, the geomechanical model was extended by a factor of ~2 along both the northern and southern edges in comparison to the fluid flow model. Addition of the extra ~2100 × 3600 feet blocks of material on the north and south ends of the reservoir flow model allows material outside of the reservoir to deform and flow in towards the reservoir in response to pressure depletion. The geologic structure for the terminal portions of these northern and southern extents were extrapolated horizontally from the geologic structure maps due to the limited lateral extent of the structure maps outside the field development.

The reservoir, which includes both diatomite and porcelanite lithologies, is discretized into nine layers (as described earlier) with a total thickness of about 1600 feet. Underlying the reservoir is the Lower Porcelanite, which is about 2200 feet thick with a vertical discretization of eight elements. As discussed above, the field data indicate that the majority of well casing damage occurs above the reservoir. Thus, the overburden, which totals about 650 feet in thickness, was more finely meshed with three stratigraphic layers and a total vertical discretization of ten elements. The three layers correspond to the Upper and Lower Tulare and the Air Sands (alluvium). Because the field data indicate that casing damage is focused at two specific horizons (immediately above the reservoir and at a second horizon some 300 feet higher in the overburden), three slip lines corresponding to known shale layers (see above discussion) were also included in the overburden. However, the slip lines were not activated for the initial geomechanical simulations reported here.

Material Models. Two simulations with the diatomite rock described by different material models were performed. In the first simulation, all thirteen layers were modeled as Drucker-Prager with a non-associated flow law and obeying the yield criterion

$$\sqrt{J_{2D}} = \kappa + \alpha J_1 \quad \text{.....(1)}$$

where α and κ are material parameters, J_{2D} is the second invariant of the deviatoric stress tensor, and J_1 is the first invariant of the stress tensor. The material parameters for the thirteen layers (**Tables 1 and 2**) were derived from conventional triaxial compression test data.[8,9]

The second simulation was performed with the upper eight layers of the diatomite reservoir described by an extended Drucker-Prager criterion which includes a second yield surface (cap) to account for inelastic compaction. The Sandia cap model is a modified version of the Weidlinger cap plasticity model.[16] Shear failure with an associated flow law occurs according to the criterion

$$\sqrt{J_{2D}} = A - C\exp(BJ_1) \quad \text{.....(2)}$$

where A, B, and C are material parameters. The cap is an elliptical surface defined by

$$\sqrt{J_{2D}} = 1/R\sqrt{[X(\xi) - L(\xi)]^2 - [J_1 - L(\xi)]^2} \quad \text{....(3)}$$

where $L(\xi)$ and $X(\xi)$ are cap position parameters with $L(\xi)= \xi$ for $\xi<0$ and $L(\xi)= 0$ for $\xi\geq 0$ and $X(\xi)$ given by

$$X(\xi) = \xi - R[A - C\exp(BL)] \quad \text{.....(4)}$$

where R is a material parameter defining the ratio of principle ellipse radii of the cap surface. The ξ is a hardening parameter defined by a functional of $X(\xi)$ and the plastic volumetric strain ε_v^p caused by cap motion

$$\bar{\varepsilon}_v^p = W[\exp\{D(X - X_0)\} - 1] \quad \text{.....(5)}$$

where $\bar{\varepsilon}_v^p$ is a history dependent functional of ε_v^p and W and D are material parameters. Plastic strain on the cap is associative with both shear and compactive components. Uniaxial strain data necessary for deriving the cap parameters (Table 2) were available for only three cycles of the diatomite, and the parameters for the remaining cycles were estimated.[9]

Boundary Conditions and Initial (Tectonic) Stresses. The four lateral edges of the geomechanical model were free to displace both vertically and in directions parallel to the boundary, but constrained from displacing perpendicular to the boundary. The bottom of the model was fixed whereas the top (i.e., surface) was free to displace in all directions. The prescribed initial tectonic stress state prior to reservoir depletion has a significant impact on the numerical results because of the non-linearity of the material models. Following Hansen *et al.*,[8] the vertical (principal) stress due to gravitational loading was calculated directly from the bulk density of the overlying materials. The initial pore pressures in the different stratigraphic layers were calculated as described in Hansen *et al.*[8] The two horizontal (principal) effective stresses, that are oriented parallel to the model boundaries, were calculated by multiplying the effective vertical stress previously computed at each individual node by factors of 0.65 and 1.20.[8] The maximum vertical surface displacement following the initial geostatic step was ~3½ inches which is considered negligible given the total model thickness (~4500 feet). The observed horizontal displacements were likewise considered insignificant.

Results of Geomechanical Simulations. Analysis of the simulation results is formidable due to the size and three-dimensionality of the model. The database consists of the x, y, and z nodal displacements and the full elemental stress tensor as a function of time (note that the x, y, and z axes do not necessarily correspond to the principal stress directions). Obviously, one can examine the simulation results from several different perspectives. Following, we show the results of three such analyses of the Drucker-Prager simulation: predicted and measured historical surface subsidence, evolution of vertical total stress and horizontal and vertical displacements at the top of the G cycle (the top interval of the diatomite reservoir), and nodal displacements along the (vertical) trajectory of one specific well. We then briefly compare the predicted surface subsidence for the Drucker-Prager and Drucker-Prager/Cap simulations.

Surface Subsidence. The simulation predicts well the overall location, shape and approximate magnitude of surface subsidence. A primary bowl aligned with the trend of the structure starts to form over the reservoir in the early 1980's, with a maximum subsidence of ~2 feet by 1985, ~ 4 feet by mid-1991, and ~4½ feet by the end of the simulation (end of 1995). The large subsidence rates predicted during the early to mid 1980's correspond to 2½ acre primary production. The continued high rates of subsidence predicted during the late 1980's (following initiation of the section-wide waterflood in 1987) are a consequence of the 1986-1990 peak in production due to a 1¼ acre infilling program conducted during 1986-87 (Fig. 5). Increased production in the southeastern part of the field during that time causes the formation of a secondary bowl in ~1987 which persists through early 1993. The reduced subsidence rates predicted in the 1990's are a consequence of the maturity of the waterflood and the reduced total production rates (as compared to the late 1980's). Cumulative subsidence on the northern and southern flanks of the geomechanical model (i.e., outside of the reservoir flow model) are ~1 foot in early 1985 and ~2 feet by the end of 1995.

Quantitative comparison of the predicted versus measured cumulative surface subsidence is complicated by both the poor monument survey coverage that existed prior to the early 1990's and also by significant uncertainties in the baseline survey data. **Fig. 6** instead compares the predicted versus measured subsidence rates. The upper left panel shows the maximum predicted subsidence rate for the entire simulation (~9 inches per year) that occurs in 1986 immediately prior to the initiation of the waterflood and that results in the formation of the secondary bowl as noted above. The predicted subsidence rates during the very late 1980's (upper right) decrease and show good agreement with the survey data that indicate rates of 2-4 inches per year (note that the time intervals for the predicted versus observed subsidence rates are not registered exactly). The secondary bowl predicted by the simulation is corroborated by the field data. The predicted subsidence rates for the following year (not shown) are nearly uniform over the entire model and are in excellent agreement with the survey data which indicate rates of 3-4 inches per year. For 1992 (lower left), the model predicts that subsidence has been nearly arrested (0-1 inch per year). This agrees reasonably well with the field data that indicates zero subsidence over much of the model area. However, the model predicts slight rebound in the upper left whereas the field data for that area indicate continued subsidence of ~1 inch per year.

The following year (lower right), the model shows increased subsidence rates in the central region of the model (above the reservoir), which is qualitatively paralleled by the field data.

Stress and Displacement at the Top of G Cycle. The effects of production- and injection-induced gradients in pore pressure on the subsurface stress and displacement field are shown in **Figs. 7-9** with plan views of the topmost layer of the diatomite reservoir (G cycle) at different times in the simulation. The spatial variation of deformation and stress in this layer is of interest since the top of the diatomite reservoir is one of the two main horizons at which well casing damage occurs. The portions of the geomechanical model that extend to the north and south of the reservoir model have been omitted from these plots for clarity. Also, note that because of the model geometry (e.g. see Fig. 1), the plots are not horizontal slices through the model. Instead, the plots are a top view of a surface which is slightly flexed (concave down) along an axis roughly perpendicular to the long dimension.

Figs. 7-9 show results for three different times, 10 years into the simulation (end of 1987, shortly after the start of the waterflood), 12 years into the simulation (end of 1989), and 18 years which is the end of the simulation (end of 1995), respectively. The first panel (A) shows the spatial variation in pore pressure. The light-colored highly elongated elliptical features are the regions surrounding hydraulic fractures that have experienced significant pressure depletion, with a maximum drawdown of about 400 psi. The corresponding dark-colored features are regions where pressures have been elevated due to water injection along hydraulic fractures. The maximum pore pressure is 770 psi, which is more than 100 psi greater than the original pore pressure prior to depletion. The second panel (B) shows the effects of the pore pressure changes on the total vertical stress. The initial total vertical stress in the G cycle prior to depletion ranged from 540 to 1090 psi, depending upon structural position. The smallest total vertical stress (405 psi) at 10 years corresponds to a production well (upper left), whereas the location and magnitude of the highest vertical stress has not changed. The third panel (C) shows the vertical nodal displacements that reveal the primary and secondary subsidence bowls discussed above. Finally, the fourth panel (D) shows the horizontal nodal x-displacements (note that the geostatic x-displacements are not corrected for in Figs. 7-9).

Fig. 8 reveals the effects of just two additional years of very aggressive injection and continued production. The reservoir pressure in the central region of the model has been depleted significantly leading to lower total vertical stresses (B) but greater effective vertical stresses, hence the large vertical compactions evident in (C). The potentially catastrophic effects of the aggressive injection in the upper left corner is dramatically revealed in (D) where along an approximately N-S oriented line, adjacent material is being displaced in opposite directions. In the topmost feature, the maximum relative horizontal displacement is ~2 feet, and in the second feature just below this, slightly under 1 foot. The aggressive injection is essentially forcing the material apart.

Fig. 9 shows the further effects of continued production and more moderate injection over an additional six years. The pore pressure field is highly varied with differences of several hundred psi occurring over very short lateral distances with a high degree of spatial correlation. The total vertical stress (B) is highly varied and mimics the well pattern with highs corresponding to injection wells and lows to production wells. Since changes in the total vertical stress parallel the changes in pore pressure (A), the variation in effective vertical stress is qualitatively similar. The maximum subsidence has shifted to the center of the model and the secondary bowl has vanished. The regions of relatively smaller vertical displacement correspond directly to the regions of high pore pressure surrounding injection wells. Lines along which material is being displaced in opposite directions are again apparent on the left half of (D).

Nodal Displacements along a Specific Well Trajectory. The field observations indicate three mechanisms for casing damage in the Belridge diatomite: shearing displacements focused over small vertical intervals in the overburden, tensional failures in the overburden, and compressional failures in the reservoir. It is thus of interest to examine the variation in horizontal and vertical displacements with depth. **Fig. 10** shows the result of such an analysis for a vertical line of nodes extending from the top of the model (surface) to its base (bottom of Lower Porcelanite). The particular line of nodes was selected to be immediately adjacent to a well and somewhat removed from the model boundaries, but was otherwise picked at random. The specific location is about ⅓ down from the north edge of the flow model and approximately midway between the east and west edges.

The top plot shows the horizontal displacement in the x-direction (parallel to the trend of the structure and the short dimension of the model) as a function of depth. The x-direction is perpendicular to the hydraulic fracture orientation, and therefore the displacement field in this direction is expected to be the most sensitive to gradients in effective stress induced by pore pressure depletion and injection. Also shown with the horizontal lines are the interfaces between the diatomite reservoir and Lower Tulare (bottom line) and between the Upper Tulare and Air Sands (top line). The maximum total horizontal displacements are ~½ foot; however, the temporal and vertical character of the displacement field contains several important features. First, the large change in mechanical properties at the interface between the diatomite reservoir and Lower Tulare introduces a sharp discontinuity in the horizontal displacement field with depth. Qualitatively, such discontinuities suggest a potential for well casing damage via a shear dog-legging mechanism. Although the observed changes in the horizontal x-displacement shown in Fig. 10 are unlikely to result in significant casing damage, we expect that activation of the slip line at this interface will amplify the magnitude of the relative offset (mechanistically, the slip lines account for thin shales

which have not been explicitly included in the geomechanical model). Our preliminary 2-D modeling with simplified geometry (i.e., flat layers) but activated slip lines shows exactly this effect.[17] The second important observation is that the minimum x-displacement actually occurs at 8 years, which is prior to the onset of water injection. That is, the waterflood, that was implemented in part to reduce the well failure risk, actually amplifies the horizontal x-displacements. During 1988-89, very aggressive injection was occurring immediately to the west of this well, so that by year 12 in the simulation (end of 1989), the G-cycle at this particular location has been pushed ~4 inches to the east. This well itself was converted from production to injection in 1988. During the final six years of the simulation, the material at this particular location has moved back ~4 inches to its original location and then continued to displace another 1½ inches in the opposite direction. During this time, the area to the west was infilled to ⅝ acre and as a result, the increased production to the west has essentially pulled material towards it.

Displacement in the horizontal y-direction (middle plot) parallel to the trend of the anticline, is substantially larger than the x-displacement, with a maximum of 1.9 feet by the end of the simulation. As discussed above, the y-direction is parallel to the hydraulic fracture orientation and hence the local perturbations in the pore pressure field do not have a strong influence. Thus, the y-displacements primarily reflect the formation of the subsidence bowl as material flows inwards in response to pressure depletion.

The bottom plot shows vertical displacements as a function of depth. Particularly significant is that the maximum vertical displacement occurs at the top of the diatomite reservoir, rather than at the surface. Thus, the differential compaction caused by production from the underlying diatomite reservoir puts the overburden in a state of relative tension. This result is qualitatively consistent with field observations of apparent tensile failures of relatively weak casing connectors used in earlier wells. Finally, the large gradient in vertical displacement which occurs in the bottom most layer of the reservoir (1-2 feet of relative offset) clearly implies a possibility for compressional well failures at great depth in the reservoir, which again agrees with field observations.

Compaction for Drucker-Prager vs. Drucker-Prager/Cap Simulations. The results of the more computationally intensive simulation using the Drucker-Prager/Cap material model to describe the diatomite are qualitatively similar to the results of the Drucker-Prager simulation described above, with the exception that significantly more vertical compaction is predicted with the former material model. **Fig. 11** shows the differential increase in the vertical nodal displacements at the top of the G cycle for the cap material model at two particular times in the simulation. The effect of the cap material model is substantial, with a maximum increase in vertical displacement of 70% at 1981 (top) and 45% at 1988 (bottom).

Reducing Well Casing Damage. The geomechanical simulations offer insight into the reservoir behavior and reveal potential locations in the reservoir and in the overburden at which well damage is most likely to occur. This information can be used to formulate improved development and operating strategies. For example, the simulations reveal the potentially catastrophic effects of the aggressive injection program conducted in 1987-89. Likewise, the simulations suggest that well failure risk should be reduced in regions of the field subjected to operating policies which are fairly continuous in space and time, e.g., injection at very high rates over short periods of time is more likely to lead to problems than is continuous injection at a reduced rate. Similarly, more regional imbalances in fluid withdrawal lead depleted areas to pull on the less depleted regions bordering them. That well casing damage is concentrated at two main horizons suggests the possibility of altering casing designs (e.g., underreaming) to guard against the large shear displacements expected at the interface between the reservoir and overburden and at other weak interfaces separating major sand units. Casing designs should also consider the tensile loading within the overburden predicted by the model. In this regard, CalResources has experienced a decline in tensile overburden failures following the use of stronger casing connectors in wells drilled after 1987. *Dale et al.* recently presented a tool for repairing sheared well casings.[18]

Conclusions

1. More than 90% of well casing damage at the Belridge Diatomite Field has occurred in the overburden. About 60-70% of the damage is focused at two depths: at the interface of the diatomite reservoir and overlying Tulare Formation and at a second horizon 300-400 feet higher in the overburden. In areas of the field experiencing significant numbers of well failures, the spatial locations of the failed wells do not correlate with macroscopic features of the subsidence bowl but instead are distributed across the entire bowl.

2. A three-dimensional non-linear finite element geomechanical model of South Belridge, Section 33 successfully reproduces the approximate magnitude, location, and shape of the subsidence bowl, as well as many details of its incremental growth.

3. The simulations reveal the evolution of the subsurface stress and displacement fields in the reservoir and overburden with time and show how local production and injection patterns affect their spatial variation. The simulations show that although the waterflood has successfully mitigated surface subsidence, it has also increased the lateral gradients in effective stress that in turn has accelerated subsurface horizontal motions.

4. The simulations suggest the three types of well casing damage observed at Belridge: shear (dog-leg) failures in the overburden, tensional failures in the overburden, and compressional failures in the reservoir. Shear failures may result from abrupt discontinuities in the horizontal displacement field at mechanical interfaces. Differential

compaction between the reservoir and overburden causes tensile stresses in the overburden that can result in well failures. Compressional failures are predicted in the diatomite reservoir where vertical compressional strains are substantial.

Nomenclature

A = material parameter, psi
B = material parameter, psi^{-1}
C = material parameter, psi
D = material parameter, psi^{-1}
E = Young's modulus, psi
J_1 = first invariant of stress tensor, psi
J_{2D} = second invariant of deviatoric stress, psi
K = Bulk modulus, psi
$L(\xi)$, $X(\xi)$ = cap position parameters
R = ratio of principle ellipse radii of cap surface
W = cap material parameter (dimensionless)
X_0 = Initial cap position, psi
T_{cut} = tension cut-off, psi
α = material parameter
ε_v^p = plastic volumetric strain
κ = material parameter, psi
ν = Poisson's ratio
ρ = bulk density, $slugs/ft^3$
ξ = cap hardening parameter

Acknowledgments

This work was supported by the US Department of Energy's Natural Gas and Oil Technology Partnership Program and was performed at Sandia National Laboratories supported by the US DOE under Contract No. DE-AC04-AL85000 and at Lawrence Berkeley National Laboratory under Contract DE-AC03-76SF00098. We also acknowledge the significant contributions of our other industry partners: CalResources (Tom Moroney, Paul Bondor), Mobil (Tony Murer), Crutcher-Tufts (Chuck Dobie), Exxon (Bruce Dale), Santa Fe Energy Resources (Kirk Broussard, Andy Lopez), Chevron (Brian Owens, Cynthia Hennigan), and Bakersfield Energy Resources (Kyle Koerner, Bob Shore). We are especially grateful to A.F. Fossum of SNL for developing and implementing the Drucker-Prager/Cap model and also thank T.A. Moroney of CalResources for providing Figs. 1 and 2.

References

1. Yudovich, A. and Morgan, D.R.: "Casing Deformation in Ekofisk," J. Petr. Tech. (July 1989) 729.
2. Bruno, M.S.: "Subsidence-Induced Well Failure," paper SPE 20058 presented at the 60th California Regional Meeting, Ventura, 4-6 April 1990.
3. Hamilton, J.M. *et al.*: "Subsidence-Induced Shear Failures Above Oil and Gas Reservoirs," *Proc. 33rd US Symp. on Rock Mechanics*, AA Balkema, Rotterdam (1992) 273.
4. Bruno, M.S. and Bovberg, C.A.: "Reservoir Compaction and Surface Subsidence Above the Lost Hills Field, California," *Proc. 33rd US Symp. on Rock Mechanics*, AA Balkema, Rotterdam (1992) 263.
5. *Oil and Gas J.*: "South Belridge 15th Billion Barrel Oil Field in US," (Oct. 1995) 119.
6. Strubhar, M.K. *et al.*: "Fracturing Results in Diatomaceous Earth Formations, South Belridge Field, California," *JPT* (March 1984) 495.
7. Myer, L. *et al.*: "Use of Visualization Techniques in Analysis of Well Failures in Diatomite Reservoirs," *The Leading Edge* (March 1996) 185.
8. Hansen, K.S. *et al.*: "Modeling Reservoir Compaction and Surface Subsidence at South Belridge," SPEPF (Aug. 1995), 134.
9. de Rouffignac *et al.*: "Subsidence and Well Failure in the South Belridge Diatomite Field," paper SPE 29626 presented at the 1992 SPE Western Regional Meeting, Bakersfield, 8-10 March.
10. Graham, S.A. and Williams, L.A.: "Tectonic, Depositional, and Diagenetic History of Monterey Formation (Miocene), Central San Joaquin Basin, California," *AAPG Bull.* (1985) **69**, No. 3, 385.
11. Schwartz, D.E.: "Characterizing the Lithology, Petrophysical Properties, and Depositional Setting of the Belridge Diatomite, South Belridge Field, Kern County, California," *Studies of the Geology of the San Joaquin Basin,* Graham (ed.), Pacific Section SEPM (1988), **60**, 281.
12. Bowersox, J.R.: "Geology of the Belridge Diatomite, Northern South Belridge Field, Kern County, California," *Structure, Stratigraphy and Hydrocarbon Occurrences of the San Joaquin Basin, California*, Kuespert and Reid (eds.) Pacific Sections of SEPM and AAPG (1990) 215.
13. McPherson, J.G. and Miller, D.D.: "Depositional Settings and Reservoir Characteristics of the Plio-Pleistocene Tulare Formation, South Belridge Field, San Joaquin Valley," *Structure, Stratigraphy and Hydrocarbon Occurrences of the San Joaquin Basin, California*, Kuespert and Reid (eds.) Pacific Sections of SEPM and AAPG (1990) 205.
14. Stone, C.M.: "SANTOS–A 2D Finite Element Program for the Quasi-static, Large Deformation, Inelastic Response of Solids," SAND90-0543, Sandia National Laboratories, Albuquerque, New Mexico (1996).
15. Biffle, J.H.: "JAC3D–A 3D Finite Element Computer Program for the Nonlinear Quasi-static Response of Solids with the Conjugate Gradient Method," SAND87-1305, Sandia National Laboratories, Albuquerque, New Mexico (1993).
16. Sandler, I.S. *et al.*: "Generalized cap model for geologic materials," *J. Geotech. Eng.* (1976) **102**, 683.
17. Hilbert, L.B. *et al.*: "2D Nonlinear Finite Element Analysis of Well Damage due to Reservoir Compaction, Well-to-Well Interactions, and Localization on Weak Layers," *Proc. 2nd No. Amer. Rock Mech. Symp.*, AA Balkema, Rotterdam (1996).
18. Dale, B.A. *et al.*: "A Case History of Reservoir Subsidence and Wellbore Damage Management in the South Belridge Diatomite Field," paper SPE 35658 presented at the 1996 SPE Western Regional Meeting, Anchorage, 22-24 May.

TABLE 1–OVERBURDEN AND PORCELANITE MATERIAL PROPERTIES (DRUCKER-PRAGER MODEL)

Material	E (psi)	ν	ρ (slugs/ft^3)	α	κ (psi)
Air Sands	18,000	0.30	3.687	0.1733	4.45
Upper and Lower Tulare	35,000	0.25	4.016	0.1398	30.63
Upper Porcelanite	68,000	0.22	3.493	0.1504	122.12
Lower Porcelanite	360,000	0.29	3.784	0.1504	122.12

TABLE 2–DIATOMITE MATERIAL PROPERTIES (DRUCKER-PRAGER AND DRUCKER-PRAGER/CAP MODELS)

Material Parameter	Diatomite G	Diatomite H	Diatomite I	Diatomite J	Diatomite K	Diatomite L	Diatomites M & N
K (psi)	24,090	31,818	42,580	33,333	36,161	56,768	82,121
$2G$ (psi)	40,769	53,846	66,554	50,000	61,196	96,068	138,974
ρ (slugs/ft^3)	3.008	3.008	3.008	3.008	3.008	3.008	3.008
α	0.1445	0.1581	0.1733	0.1621	0.1638	0.2310	0.3141
κ (psi)	86.57	83.85	80.81	72.26	82.71	85.55	65.04
A (psi)	5,124,687.6	5,124,687.6	5,124,687.6	5,124,680.2	5,124,686.0	5,124,700.0	4,693,116.0
B (psi^{-1})	2.820E-8	3.085E-8	3.381E-8	3.162E-8	3.196E-8	4.510E-8	6.690E-8
C (psi)	5,124,572.1	5,124,572.1	5,124,572.2	5,124,579.8	5,124,570.0	5,124,570.0	4,692,973.0
D (psi^{-1})	2.67E-8	8.867E-8	3.536E-8	1.837E-8	1.412E-8	2.560E-8	9.870E-8
R	1.7147	1.7147	1.7667	1.559	1.559	1.195	1.195
W	922.1	266.4	4486.8	2335.3	535.1	198.6	45.2
X_0 (psi)	-207	-207	-213	-162	-186	-183	-183
T_{cut} (psi)	400	365	333	310	354	309	228

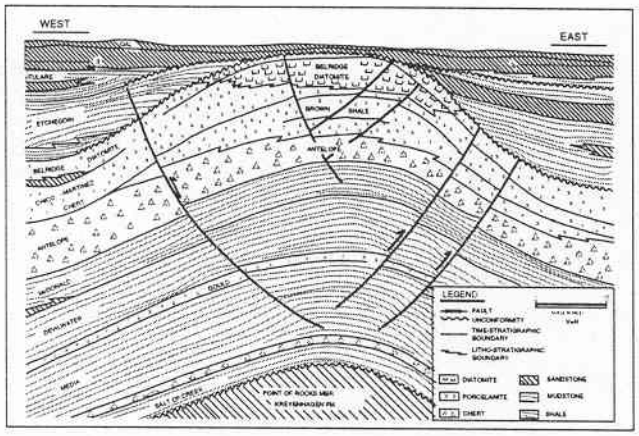

Fig. 1–Geologic east-west cross section of South Belridge Field.

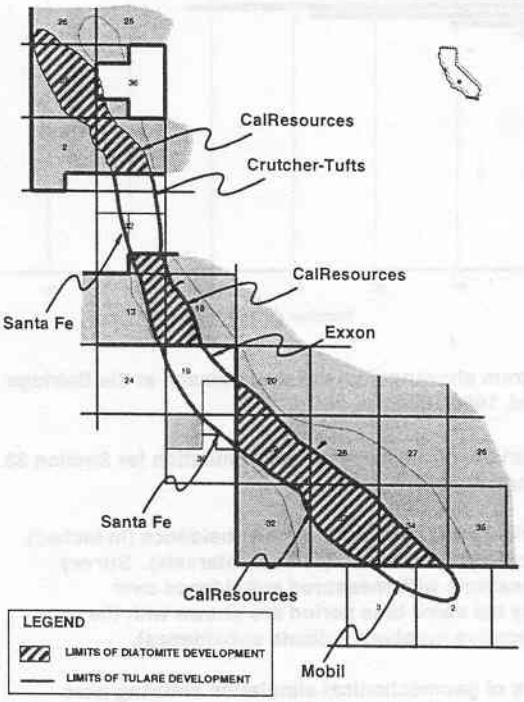

Fig. 2–Belridge Field showing lease locations for the five operators.

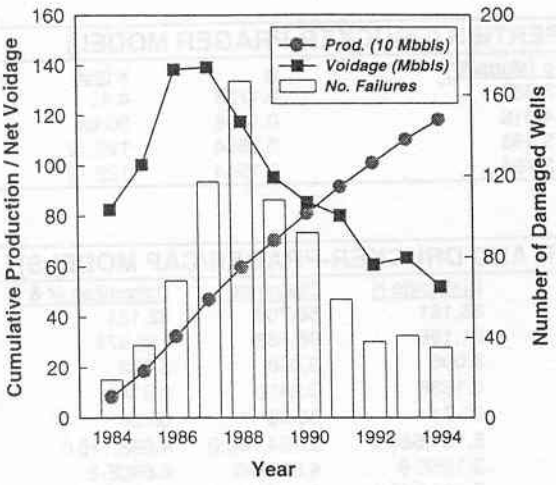

Fig. 3–Annual production, net voidage, and well failures for the Belridge diatomite field, 1984-1994.

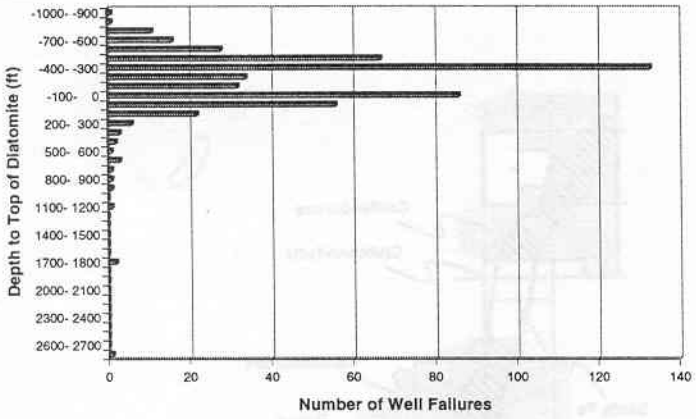

Fig. 4–Histogram showing depth of well damage at the Belridge diatomite field, 1984-1994.

Fig. 5–Comparison of the 3D reservoir simulation for Section 33 with the historical performance.

Fig. 6–Numerical prediction of surface subsidence (in inches) over the indicated time periods (~1 year intervals). Survey monument locations with measured subsidence over approximately the same time period are shown with the diamonds (negative numbers indicate subsidence).

Fig. 7–Results of geomechanical simulation showing pore pressure (A), total vertical stress (B), vertical nodal displacement (C), and horizontal *X*-displacement (D) at the top of the G cycle at 8 years into the simulation.

Fig. 8–Results of geomechanical simulation at 12 years (see Fig. 7).

Fig. 9– Results of geomechanical simulation at 18 years (see Fig. 7).

Fig. 11–Differential vertical subsidence at the top of G cycle (in feet) for the simulations using the Drucker-Prager and Drucker-Prager/Cap models for the diatomite rock at 3 years (top) and 10 years (bottom).

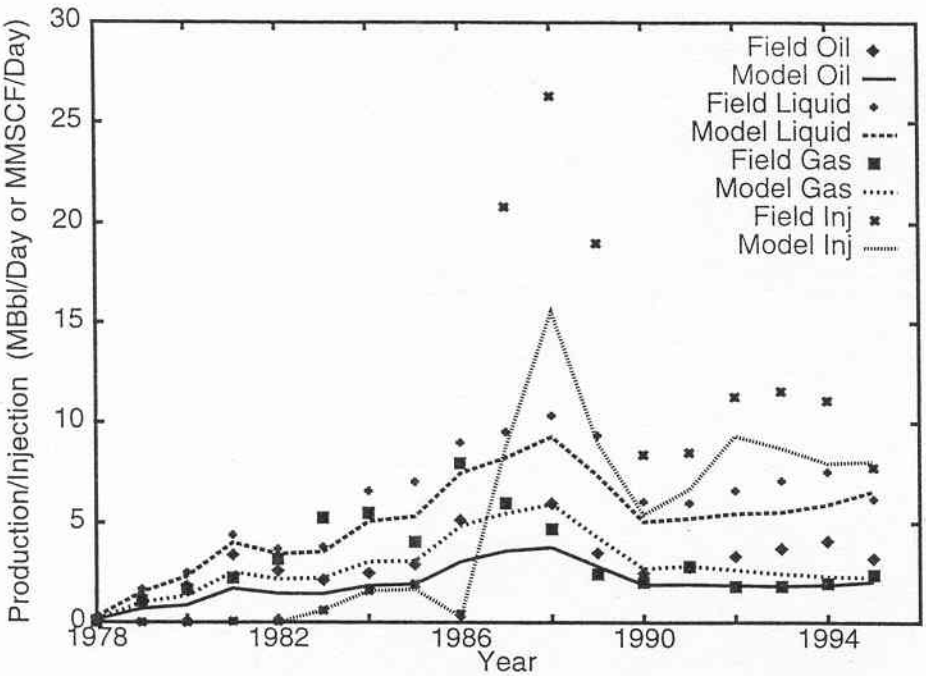
Production/Injection (MBbl/Day or MMSCF/Day)
30
25
20
15
10
5
0
1978
1982
1986
1990
1994
Year
Field Oil
Model Oil
Field Liquid
Model Liquid
Field Gas
Model Gas
Field Inj
Model Inj

Figure 5

Figure 6

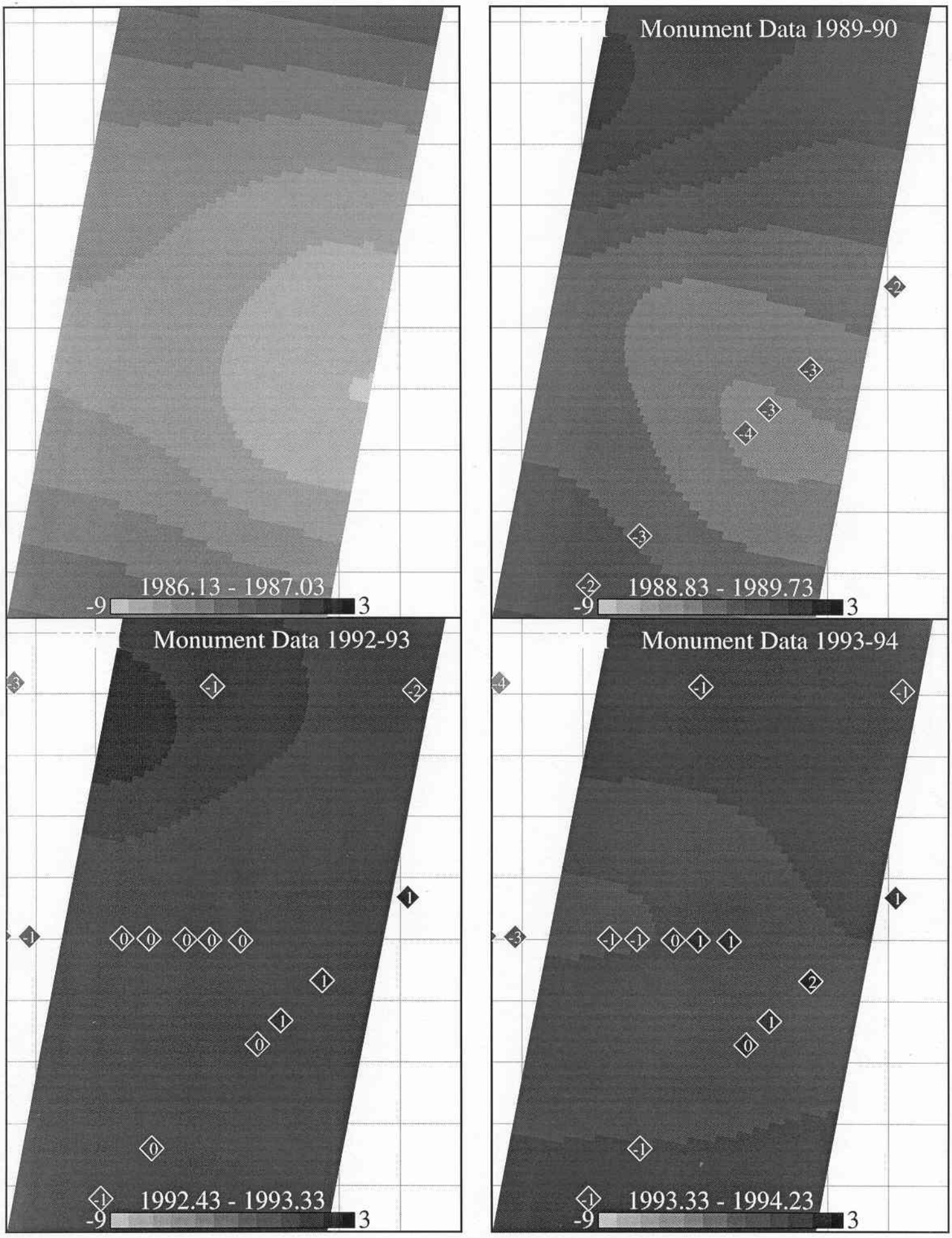
1986.13 - 1987.03
-9
3
Monument Data 1989-90
1988.83 - 1989.73
-9
3
Monument Data 1992-93
1992.43 - 1993.33
-9
3
Monument Data 1993-94
1993.33 - 1994.23
-9
3

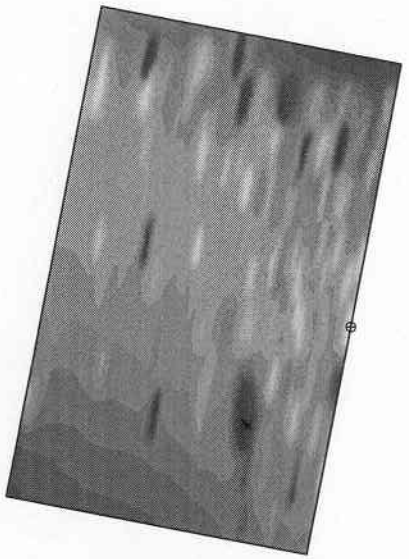

MAGNIFIED BY 1.000
ELEMENT BLOCKS ACTIVE:
1 OF 29

Pore Pressure (psi)

0.030E+3
0.590E+3
1.150E+3

⊕ = 85.9
✳ = 769.5

TIME 9.938

(A)

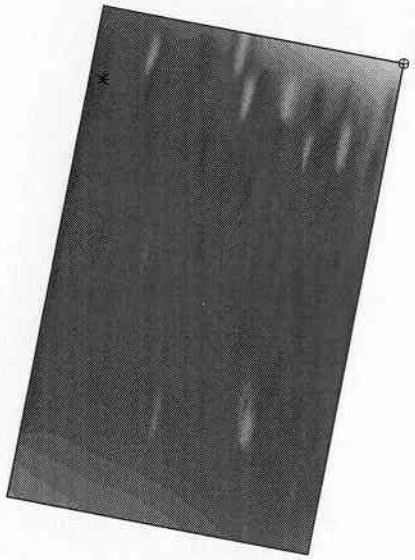

MAGNIFIED BY 1.000
ELEMENT BLOCKS ACTIVE:
1 OF 29

Vertical Stress (psi)

-1.220E+3
-0.700E+3
-0.180E+3

⊕ = -1.105E+3
✳ = -0.405E+3

TIME 9.938

(B)

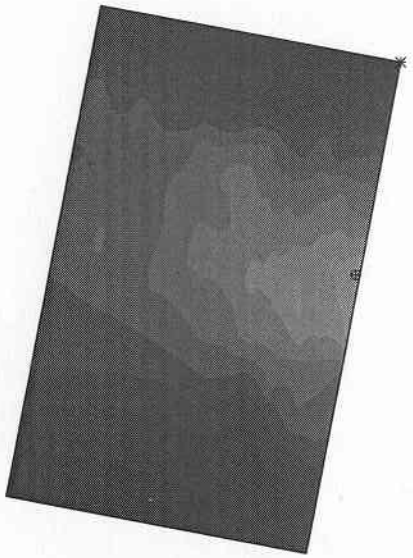

MAGNIFIED BY 1.000
ELEMENT BLOCKS ACTIVE:
1 OF 29

Vertical Displacement (ft)

-5.100
-2.300
0.500

⊕ = -3.292
✳ = -0.819

TIME 9.938

(C)

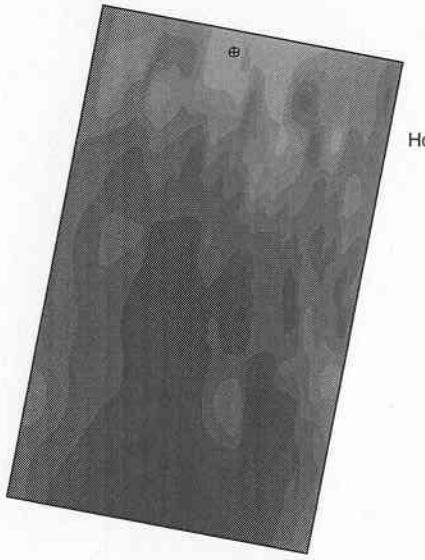

MAGNIFIED BY 1.000
ELEMENT BLOCKS ACTIVE:
1 OF 29

Horizontal X–Displacement (ft)

-0.935
0.225
1.385

⊕ = -0.3700
✳ = 0.3948

TIME 9.938

(D)

figure 7

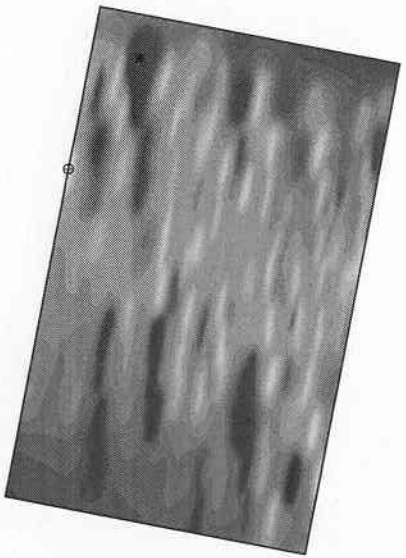

MAGNIFIED BY 1.000
ELEMENT BLOCKS ACTIVE:
1 OF 29

Pore Pressure (psi)

0.030E+3
0.590E+3
1.150E+3

⊕ = 101.3
✳ = 872.4

TIME 12.64

(A)

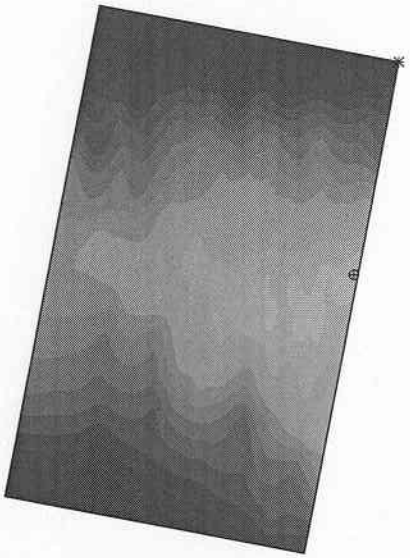

MAGNIFIED BY 1.000
ELEMENT BLOCKS ACTIVE:
1 OF 29

Vertical Displacement (ft)

-5.100
-2.300
0.500

⊕ = -3.990
✳ = -1.011

TIME 12.64

(C)

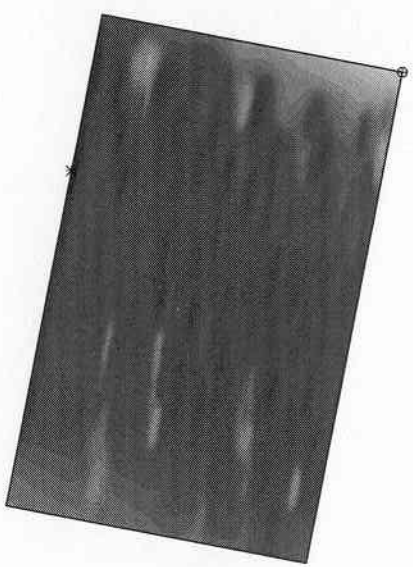

MAGNIFIED BY 1.000
ELEMENT BLOCKS ACTIVE:
1 OF 29

Vertical Stress (psi)

-1.220E+3
-0.700E+3
-0.180E+3

⊕ = -1.091E+3
✳ = -0.370E+3

TIME 12.64

(B)

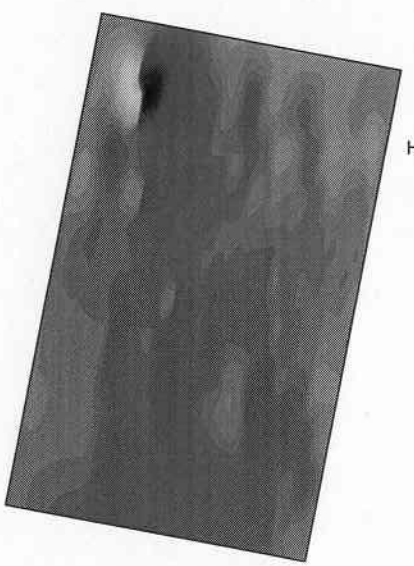

MAGNIFIED BY 1.000
ELEMENT BLOCKS ACTIVE:
1 OF 29

Horizontal X-Displacement (ft)

-0.935
0.225
1.385

⊕ = -0.803
✳ = 1.314

TIME 12.64

(D)

Figure 8

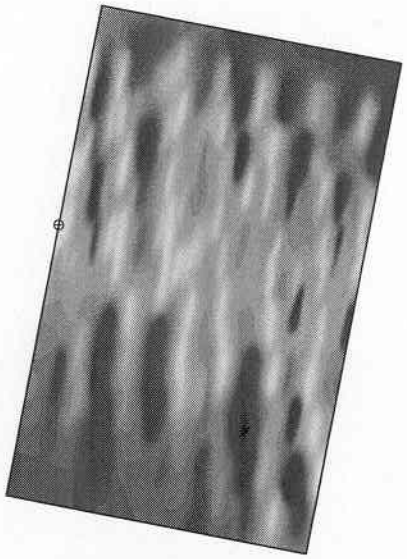

MAGNIFIED BY 1.000
ELEMENT BLOCKS ACTIVE:
1 OF 29

Pore Pressure (psi)

0.030E+3
0.590E+3
1.150E+3

⊕ = 53.9
✳ = 927.6

TIME 18.00

Y
Z
X

(A)

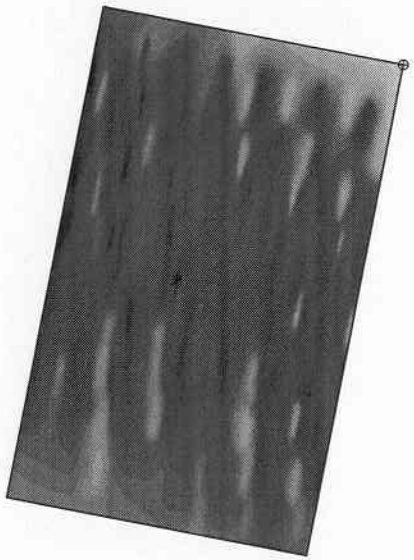

MAGNIFIED BY 1.000
ELEMENT BLOCKS ACTIVE:
1 OF 29

Vertical Stress (psi)

-1.220E+3
-0.700E+3
-0.180E+3

⊕ = -1.089E+3
✳ = -0.318E+3

TIME 18.00

Y
Z
X

(B)

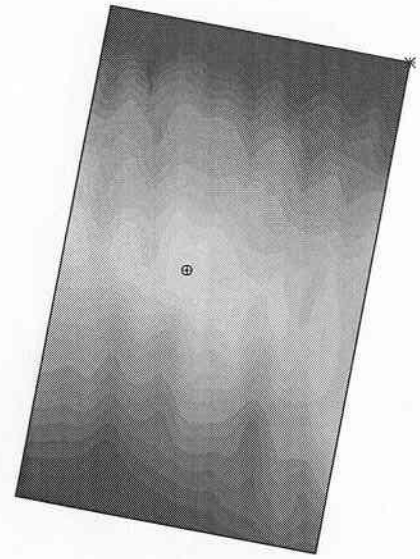

MAGNIFIED BY 1.000
ELEMENT BLOCKS ACTIVE:
1 OF 29

Vertical Displacement (ft)

-5.100
-2.300
0.500

⊕ = -4.787
✳ = -1.104

TIME 18.00

Y
Z
X

(C)

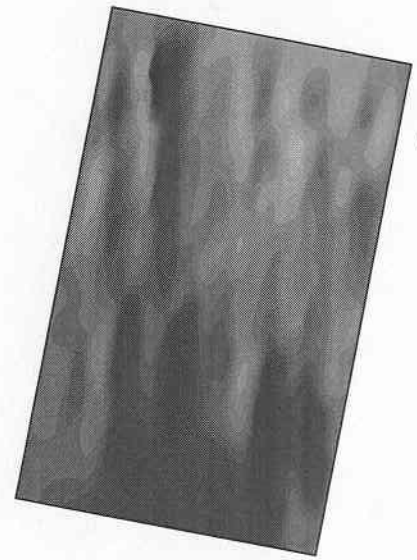

MAGNIFIED BY 1.000
ELEMENT BLOCKS ACTIVE:
1 OF 29

Horizontal X–Displacement (ft)

-0.935
0.225
1.385

⊕ = -0.5590
✳ = 0.6314

TIME 18.00

Y
Z
X

(D)

Figure 9

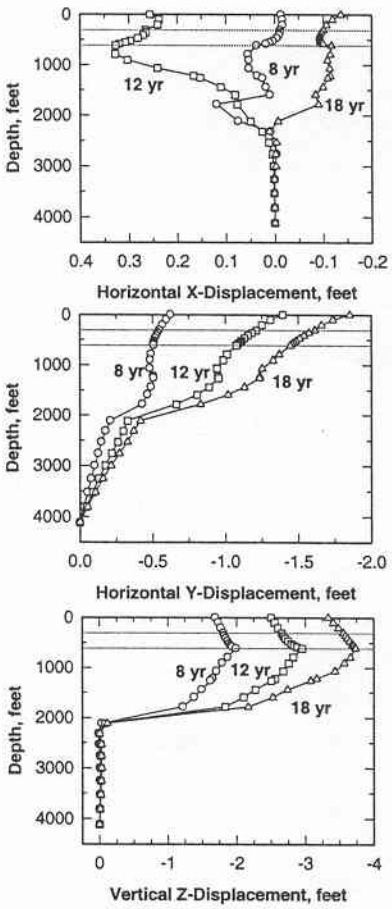

Fig. 10–Nodal displacements at a particular well location.

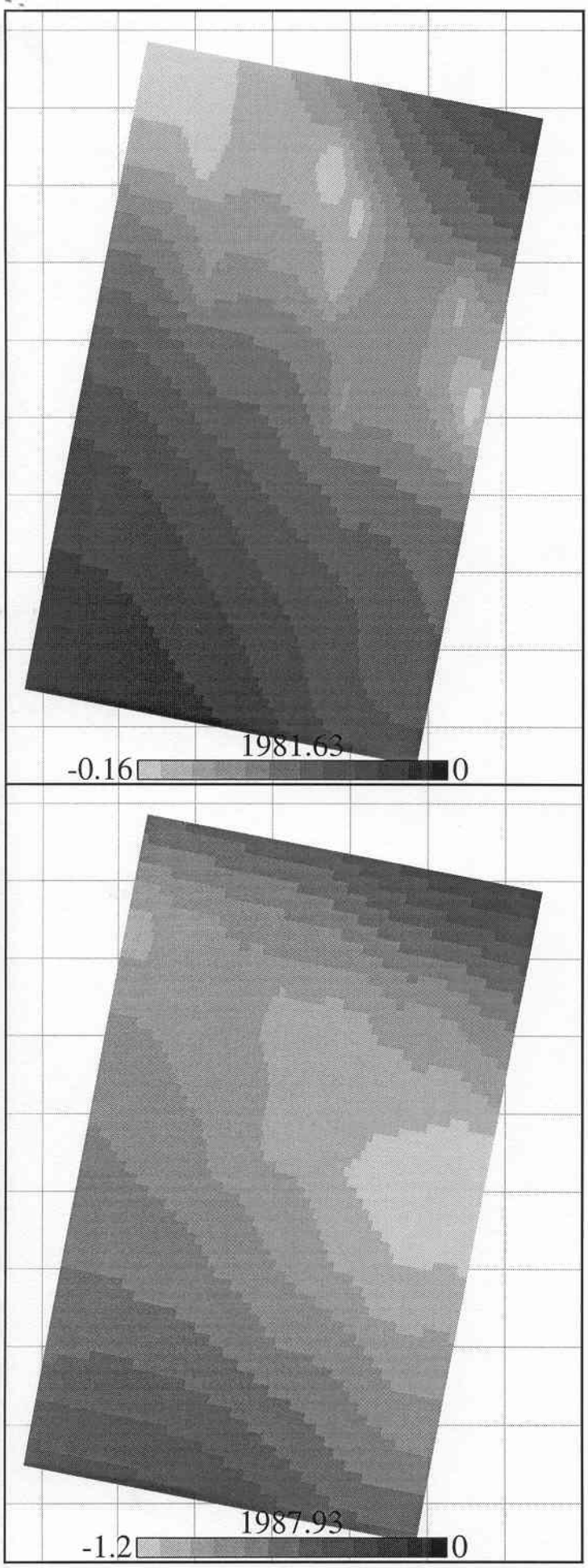

Figure 11